NeuroImage 125 (2016) 895–902

Contents lists available at ScienceDirect

NeuroImage

journal homepage: www.elsevier.com/locate/ynimg

Visualization of perivascular spaces in the human brain at 7 T: sequence optimization and morphology characterization

Xiaopeng Zong *, Sang Hyun Park, Dinggang Shen, Weili Lin

Department of Radiology and BRIC, University of North Carolina at Chapel Hill, Chapel Hill, NC 27599, USA

ARTICLE INFO

Article history:
Received 21 June 2015
Accepted 26 October 2015
Available online 28 October 2015

Keywords:
Perivascular spaces
Variable flip angle
Turbo spin echo
MPRAGE
7 T
MRI
Virchow–Robin space

ABSTRACT

Noninvasive imaging of perivascular spaces (PVSs) may provide useful insights into their role in normal brain physiology and diseases. Fast MRI sequences with sub-millimeter spatial resolutions and high contrast-to-noise ratio (CNR) are required for accurate delineation of PVS in human. To achieve the optimal condition for PVS imaging at 7 T, we carried out detailed simulation and experimental studies to characterize the dependence of CNR on imaging sequences (T_1 versus T_2-weighted) and sequence parameters. In addition, PVSs were segmented semi-automatically, which revealed much larger numbers of PVSs in young healthy subjects (age 21–37 years) than previously reported. To the best of our knowledge, our study provides, for the first time, detailed length, volume, and diameter distributions of PVS in the white matter and subcortical nuclei, which can serve as a reference for future studies of PVS abnormalities under diseased conditions.

Introduction

Perivascular spaces (PVSs), also known as the Virchow–Robin spaces, are fluid-filled spaces surrounding penetrating arteries and veins in the brain (Esiri and Gay, 1990). While enlarged PVSs are commonly observed in MR images in a number of neurological disorders (Conforti et al., 2013; Doubal et al., 2010; Inglese et al., 2005; Li et al., 2014; Potter et al., 2013; Rouhl et al., 2012; Wardlaw, 2010), normal PVSs are typically not visible due to their small sizes, particularly in young adults; histopathological findings have suggested a positive relation between the dimensions of PVS and age (Pesce and Carli, 1988). However, the physiological and pathophysiological significances of PVS remain elusive. Recently, several lines of evidence have suggested that PVS is a part of the brain "lymphatic" system through which interstitial solutes are cleared from the brain (Iliff et al., 2013; Kress et al., 2014; Rangroo Thrane et al., 2013; Yang et al., 2013). Specifically, it has been demonstrated that arterial pulsation drives subarachnoid cerebral spinal fluid (CSF) flow into the PVS, clearing soluble proteins such as amyloid beta (Aβ) from the brain (Bilston et al., 2003; Iliff et al., 2013). Dysfunction of PVS pathways thus may lead to enlarged PVS, increased Aβ deposition, and subsequent neuronal dysfunction and loss, which clearly have profound implications in Alzheimer's disease (Iliff et al., 2012; Yang et al., 2013). While these recent studies have provided invaluable insights into the functions of PVS for cleaning interstitial solutes, they employed invasive approaches such as two-photon microscopy or infusion of fluorescent and radio-labeled tracers that are not applicable to humans (Iliff et al., 2013; Kress et al., 2014; Rangroo Thrane et al., 2013; Yang et al., 2013).

Noninvasive imaging of PVS morphology may provide important insights into the functional status of PVS. Both T_1- and T_2-weighted MRI sequences have been employed for imaging PVS (Bouvy et al., 2014; Maclullich et al., 2004; Wuerfel et al., 2008; Zhu et al., 2011). However, previously reported results have largely focused on abnormal ("dilated" or "enlarged") PVS using relatively low-resolution images with respect to the diameters of normal PVSs which are typically in the range of 0.13–0.96 mm, with the majority below 0.5 mm (Pesce and Carli, 1988). As a result, the normal morphological features of PVS remain elusive. The increased signal-to-noise ratio (SNR) at 7 T enables acquisition of high resolution anatomical images and could potentially enhance our ability to discern normal patterns of PVS beyond those reported at a lower magnetic field (Bouvy et al., 2014; Maclullich et al., 2004; Wuerfel et al., 2008). Bouvy et al. reported normal PVS at 7 T using isotropic spatial resolutions of $0.5 \times 0.5 \times 0.5\ mm^3$ and $0.7 \times 0.7 \times 0.7\ mm^3$ with magnetization prepared rapid gradient echo (MPRAGE) and T_2-weighted variable flip angle (VFA) turbo spin echo (TSE) sequences, respectively (Bouvy et al., 2014). However, it is unclear if the resolutions employed by Bouvy et al. were sufficient to clearly delineate normal PVS, nor is it clear if the imaging parameters were optimized. Furthermore, quantitative measures of morphological features, such as length or diameter distributions, were not provided. To this end, we carried out both simulation and experimental studies to optimize imaging parameters of the MPRAGE and VFA-TSE sequences (Busse et al., 2006;

* Corresponding author.
E-mail addresses: zongxp@gmail.com (X. Zong), shpark13135@gmail.com (S.H. Park), dgshen@med.unc.edu (D. Shen), weili_lin@med.unc.edu (W. Lin).

http://dx.doi.org/10.1016/j.neuroimage.2015.10.078
1053-8119/

Mugler and Brookeman, 1990) to maximize contrast-to-noise ratio (CNR) for PVS at 7 T. Specifically, simulations were carried out to study the sequence parameter dependence of PVS to white matter (WM) contrast in T_1 and T_2-weighted sequences. Subsequently, the sequence with the imaging parameters that provided the highest CNR was employed to image PVS, which in turn enabled segmentation of PVS over the whole imaging volume using a semi-automatic method. Finally, we analyzed the morphological features of extracted PVS, including diameter, length, and volume distributions over the WM and subcortical nuclei including basal ganglia and thalamus.

Methods and materials

A total of 7 healthy volunteers were recruited (ages 21–37). The study was approved by local institutional review board and written consents were obtained from all subjects. All images were acquired on a 7 T Siemens scanner using a 32-channel receive head coil and a single-channel volume transmit coil (Nova Medical, Wilmington, MA). Due to the known B_1 inhomogeneity at 7 T (Vaughan et al., 2001), the transmitter voltage was calibrated such that the flip angle (FA) matched with the true FA at the center region of the brain. The first subject was scanned for measurement of T_1 and T_2 values of CSF and WM which are needed for simulation and calculating the variable flip angles of the TSE sequence. Subsequently, simulation was carried out based on the measured T_1 and T_2 values for further optimization. Afterwards, 6 subjects were scanned with the optimized parameters to study the morphological features of PVS as well as to confirm the simulated dependence of PVS–WM contrast on echo time in the TSE weighted sequence.

Sequence parameter optimization

Experiments

T_1 and T_2 maps were first acquired with a single-slice TSE sequence in one subject to obtain estimates of T_1 and T_2 in CSF and WM. The following sequence parameters were used: voxel size $= 0.5 \times 0.5 \times 2\ mm^3$, matrix size $= 448 \times 360$, refocusing FA $= 180°$, and one axial slice cutting through the middle of the occipital lobe. For T_1 mapping, the echo train length (ETL) was 8, and six images with TR of 254, 500, 1000, 2000, 4000, and 8000 ms were acquired. For T_2 mapping, due to the large difference in T_2 between CSF and brain parenchyma, two multi-TE TSE scans were performed with relatively long and short TE values, respectively. Specifically, TE values of 912, 760, 608, 456, 304, and 76 ms together with TR = 3000 ms, and ETL = 12 for each image were used for measuring T_2 of CSF, whereas TE values of 183, 148, 113, 78, 44, and 8.7 ms with TR = 2000 ms and ETL = 4 were used for measuring T_2 of brain parenchyma.

Simulation

Numerical simulations were performed to calculate the PVS–WM contrast for both MPRAGE and TSE sequences. The MPRAGE signal after each readout RF pulse was obtained through Bloch simulation by taking into account the effects of all preceding RF pulses and T_1 relaxation and assuming a complete inversion by the adiabatic inversion pulse. The TSE signal was simulated with the extended phase diagram algorithm (Hennig, 1988). For PVS, $T_1 = 3500$ ms and $T_2 = 600$ ms, while for WM, $T_1 = 1360$ ms and $T_2 = 75.3$ ms, as experimentally measured in CSF and WM regions of interest (ROI) in the first subject. The contrast between PVS and WM was taken as the simulated signal difference at k-space center. The simulated signals were weighted by the water contents which were assumed to be 1 and 0.71 for PVS and WM, respectively, for MPRAGE (Whittall et al., 1997). In contrast, water contents of 1 and 0.63 for PVS and WM were used for TSE due to the fact that the T_2 of myelin water was too short to be detected in our TSE sequence and was thus excluded (Laule et al., 2008; Whittall et al., 1997). All sequence parameters in the simulation were the same as described for the experiments in the next section, unless otherwise specified.

The B_1 field with a single channel transmit coil is known to be inhomogeneous at 7 T, i.e., with B_1 at the edge of the brain ~42.5% lower than that at the center (Vaughan et al., 2001). Such a B_1 inhomogeneity might be most detrimental to TSE sequences as the effects of incorrect B_1 can accumulate along the echo train. The B_1 reduction is expected to reduce image intensity and PVS–WM contrast in TSE images. To study the degree of reduction, the simulations were repeated with flip angles that were scaled from their ideal values with a scaling factor ranging between [0.58, 1]. All other parameters were kept constant and the same as those in the experiments.

To find the optimal TI and FA values in the T_1-weighted MPRAGE sequence, the sequence was simulated at different inversion times (TIs) and FAs. To find the optimal TE in the TSE sequence, the sequence was simulated at different TEs while keeping the RF power constant (Busse et al., 2006). The RF power was calculated as the sum of squares of the FAs of all RF pulses in a repetition. The powers for different TEs were kept constant by adjusting the pseudo-steady-state magnetization (M_{pss}) in the echo train (Busse et al., 2006). The total RF power and M_{pss} matched with those in the experiments. The pseudo-steady-state was maintained until the data for $k_y = 0$ (where k_y is the k-space coordinate along the first phase encoding direction) was acquired, which provided a good balance between SNR and spatial resolution requirements (Busse et al., 2006).

PVS contrast and morphology study

Six subjects were scanned with the MPRAGE and VFA-TSE sequences for PVS imaging, as well as a magnetization prepared double rapid acquisition gradient echo (MP2RAGE) sequence (Marques et al., 2010) for segmenting different brain tissues. The common imaging parameters of the three sequences are listed in Table 1. As a linear phase encoding scheme was used in the VFA-TSE sequence, the echo train was shorter at smaller TE, thus allowing the application of higher flip angles and also the achievement of higher M_{pss} within the SAR safety limit. The M_{pss} was set at 0.544, 0.475, and 0.42, respectively, keeping the SAR at about 78% of the scanner's safety limit for all three TE values (Table 1). Note that no interpolation was performed during the reconstruction, so that the matrix sizes were identical between the acquired and reconstructed images. The field of view covered the entire centrum semiovale and basal ganglia, while excluding the inferior part of the temporal lobe.

Data analysis

A T_1 map was obtained from the T_1 data by fitting the image intensity versus TR in each voxel using the equation: $s(TR) = M_0(1-\alpha \cdot e^{-TR/T_1})$

Table 1
MRI parameters for the MPRAGE, VFA-TSE, and MP2RAGE sequences.

	MPRAGE	VFA-TSE	MP2RAGE
TE (ms)	3.67	319/500/707	1.89
TR (ms)	5000	5000	6000
Echo spacing (ms)	6	8.62	5.7
Matrix size	512*400*256	512*404*208	308*304*256
Resolution (mm^3)	0.41*0.41*0.4	0.41*0.41*0.4	0.65*0.65*0.65
FA (degree)	8	Variable	4 (TI1), 4 (TI2)
Slice orientation	sagittal	Axial	sagittal
TI (ms)	1800	N.A.	800/2700
Partial Fourier factor	1 (PE1); 1 (PE2)	0.69/0.84/0.98 (PE1);0.75 (PE2)	0.75 (PE1); 0.75 (PE2)
GRAPPA factor	3 (PE1)	3 (PE1)	3 (PE1)
Auto calibration Lines	24	30	32
Bandwidth (Hz/Pixel)	700	349	290
TA (min)	12:25	13:00	9:42
Flow compensation	Read	Read	None

with three free parameters M_0, α, and T_1 (Conturo et al., 1987). For the T_2 data, the signal intensity versus TE was fit with a single exponential decay to obtain T_2. ROIs were separately placed in the WM and CSF to obtain estimates of their mean T_1 and T_2 values. Fig. 1 displays the measured T_1 and T_2 maps together with the CSF (green) and WM (red) ROIs. It is interesting to note that Fig. 1 shows apparent differences in T_2 among the four WM ROIs, likely due to an orientation dependence of WM T_2 values (Bender and Klose, 2010; Lee et al., 2011). The mean T_1 and T_2 values obtained from these ROIs were used for the WM and CSF, respectively, in the simulation.

The TSE images at different TEs were aligned using the 3dvolreg function in AFNI (Cox, 1996), which has been widely used for image registration in the functional MRI studies, while the MPRAGE images were manually aligned to the TSE images in the AMIDE image analysis tool (Brown et al., 2002). To calculate the CNR between WM and PVS, ROIs were defined in large PVS that were at least 3 voxels wide, within the surrounding WM, and outside the skull for calculating their mean signals (denoted as S_{PVS}, S_{WM}, and S_{bg}). As we were only concerned on comparing the CNR among sequences, a relative CNR was defined as $rCNR = (S_{WM} - S_{PVS})/S_{bg}$. To compare the TE and sequence dependences of rCNR with simulation, rCNRs were normalized to the value in the TSE image with TE = 319 ms.

To study the morphological features of the PVS, a semi-automatic PVS extraction method was developed and applied to the images with the highest rCNR (i.e., TSE images with TE = 319 ms). The method consists of the following steps: First, we extracted WM from the MP2RAGE images to minimize the chance of misidentifying thin tubular structures in the skull and GM as PVS. Specifically, skull stripping was conducted on the normalized MP2RAGE images by using the Brain Extraction Tool (Smith, 2002) after correcting intensity inhomogeneity with the N3 correction method (Sled et al., 1998). The brain tissues were classified into WM, GM, and CSF regions by using the FAST method, with the partial volume estimation option off (Zhang et al., 2001). The WM region was then reduced with a morphological shrinking algorithm to exclude tubular structures on the boundaries between WM and cortex. Finally, the FSL-FLIRT tool (Jenkinson et al., 2002) was used to register the TSE and MP2RAGE images by using mutual information similarity. Second, we extracted all possible thin tubular structures in WM and subcortical nuclei by using Frangi's vesselness filter (Frangi et al., 1998). Specifically, we employed a Gaussian kernel to smooth the image, and then computed the eigenvalues of the Hessian matrices of the smoothed image. The vesselness of each voxel was estimated by the relationship between the three eigenvalues representing principal directions. More details can be found in (Frangi et al., 1998). To find

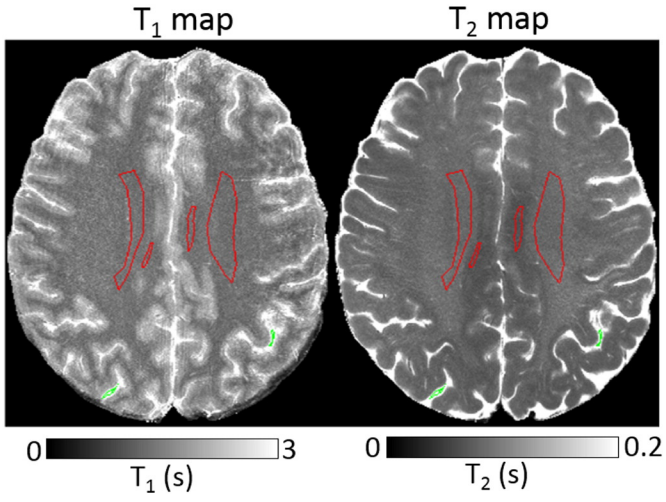

Fig. 1. Regions of interest (ROIs) for calculating the mean T_1 and T_2 values in WM and CSF. The red and green contours enclose the WM and CSF ROIs, respectively. The underlying images are the measured T_1 and T_2 maps.

all thin tubular structures with different diameters, we used multiple values of standard deviation (i.e., 1, 2, 3 and 4 voxels) in the Gaussian kernel and chose the maximum vesselness value among different degrees of smoothing as the final vesselness. We then defined the voxels with high vesselness (i.e., larger than a certain threshold) as tubular structures. To minimize the number of missing PVSs, the threshold was heuristically set as a low value in this step, although some incorrect structures were also detected. Third, we removed structures with length less than 0.8 mm or greater 30 mm. Note that the lower limit of 0.8 mm was chosen so that the PVS path was at least 2 voxels long, while the upper limit was chosen heuristically as the majority of PVS in our data were below 20 mm (see Fig. 7(A) below). Finally, we manually corrected the remaining erroneous cases (i.e., recovering some missing PVS and removing outliers) by using ITK-SNAP (Yushkevich et al., 2006) and the neurite tracer plugin in ImageJ (Longair et al., 2011).

After PVS segmentation, each connected cluster was defined as one PVS. A thinning algorithm was then applied to each cluster for defining the path (Laule et al., 2008; Whittall et al., 1997) and the PVS path was determined to be the longest pathway between any two voxels within the thinned cluster. PVS diameter was calculated for each voxel on the path (VoP) by counting the number of voxels in the original cluster that were closer to that voxel than to any other VoP. Then, the diameter was calculated as:

$$D = 2\sqrt{N \times (0.4\text{mm})^3 / l\pi} \quad (1)$$

where N was the number of voxels associated with that VoP, and l was the mean distance of the VoP to its two neighboring VoPs. The terminal VoPs were excluded for diameter analysis since their diameters were artificially increased due to the thinning algorithm.

To study the possible spatial variations of the PVS morphology, the WM were divided into frontal (FL), parietal–occipital (POL), and temporal lobes (TL). Then, all PVSs were assigned to FL, POL, TL, or subcortical nuclei (SN) (including basal ganglia and thalamus). The PVSs intersecting with multiple regions were assigned to the region with the most voxels of the PVS. We also calculated the volume fraction of PVSs in each region as the total volume of PVS in the region divided by the total volume of the region.

To study the variation of PVS diameters along the path, normalized distance was calculated for each VoP so that the results from different PVS can be combined. The normalized distance was defined as the path distance from the VoP to one of the terminal VoP normalized by the total path length of the PVS. The terminal VoP for the calculation was chosen to be the one closest to the brain surface and most inferior for the WM and SN PVS, respectively, such that the direction of increasing normal distance coincided with the direction of arterial blood flow inside the PVS. The VoPs in FL and POL were binned into twenty segments according to their normalized distances: (0, 0.05), [0.05, 0.1), … [0.95, 1). Due to the much smaller numbers of segmented PVS in TL and SN, the bin intervals were (0, 0.1), [0.1, 0.2), … [0.9, 1) in these two regions. Finally, the mean diameter of each segment was calculated in each subject by averaging the diameters of all VoPs in that segment.

Results

Simulation

Figs. 2(A) and (B) show examples of the simulated evolution of the echo train signals in PVS and WM for the MPRAGE and TSE sequences, respectively. Here, the MPRAGE was simulated with TI = 1800 ms and FA = 8°. The contrasts calculated as the signal differences between PVS and WM at the echo for $k_y = 0$ are denoted by the vertical lines. It is evident that the maximum contrast in the TSE sequence is ~10 times higher than that in the MPRAGE sequence, indicating that TSE sequences are more suitable for imaging the PVS. Fig. 2(C) shows the

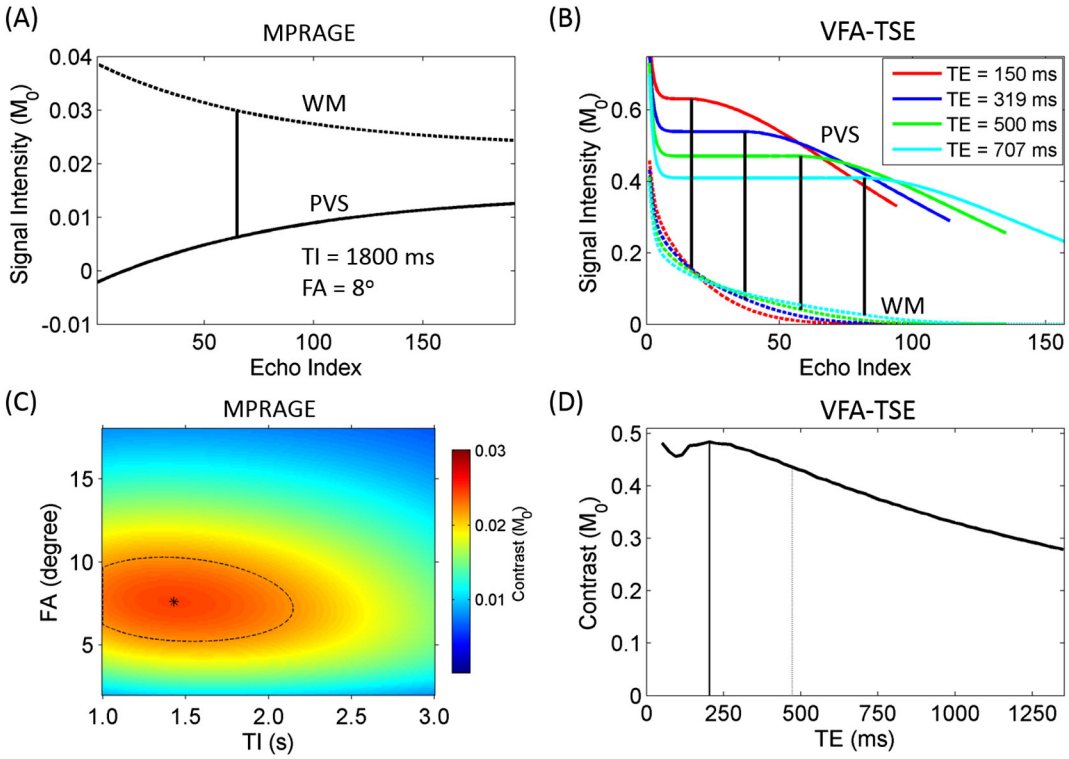

Fig. 2. (A) Simulated gradient echo signal evolutions in MPRAGE sequence with TI = 1800 ms and FA = 8°. The dashed and solid lines correspond to WM and PVS, respectively. The black vertical line denotes the signal difference between WM and PVS at $k_y = 0$. (B) Simulated echo signal evolutions in the VFA-TSE sequence with different TE but fixed total RF power. The meanings of the colored dashed, colored solid, and black vertical lines are the same as in (A). (C) Dependence of PVS–WM contrast on FA and TI in the MPRAGE sequence. The black contour shows the region with the contrast greater than 90% of the maximum value, and the location with the maximum contrast is denoted by an asterisk. (D) Dependence of PVS–WM contrast on TE in the VFA-TSE sequence with the total RF power the same as in the experiment. The vertical solid and dashed lines denote the TE values with contrasts equaling to 100% and 90% of the maximum value, respectively.

dependence of the PVS–WM contrast on TI and FA in the MPRAGE sequence, where the region with >90% of the maximum contrast is denoted by the black contour and the location with maximum contrast by an asterisk. There is a large region in the FA–TI plane with TI ⊂[1.0, 2.0] s and FA ⊂[5°, 11°] where the contrast is relatively constant (<10% change). Fig. 2(D) plots the PVS contrast as a function of TE in the TSE sequence. The vertical dashed line denotes the TE range (TE < 473 ms) with the contrast of less than 10% difference to the peak value and the vertical solid line denotes the TE value (204 ms) with maximum contrast.

Fig. 3 shows the simulated dependence of the PVS–WM contrast on the B_1 scaling factor. An approximately linear decrease of the PVS–WM contrast with decreasing B_1 for the TSE sequences is observed, while the reduction is much less for the MPRAGE sequence. At the smallest B_1 scale of 0.52, the contrast is reduced from the ideal case by 56%, 55%, and 54% for TSE with TE = 319, 500, and 707 ms, respectively. While at the same B_1 scale, the reduction is only 16% for MPRAGE.

Relative contrast-to-noise ratio (rCNR)

Fig. 4 shows both the measured rCNR and simulated contrast for the MPRAGE and the TSE images after normalization by their values at TE = 319 ms. The MPRAGE images had a lower rCNR than TSE images. Regarding the dependence on TE for TSE, TE = 319 ms exhibited the highest rCNR, which progressively decreased with increasing TE. The measured rCNR in TSE was lower than the simulated contrasts at the two longer TEs. This discrepancy is most likely attributed to the increased susceptibility to motion with increasing echo train duration at a longer TE. On the other hand, the measured rCNR was greater than the simulated contrast for the MPRAGE sequence, which could be explained by the decreased dependence on B_1 inhomogeneity for the MPRAGE sequence (see Fig. 3). The increased rCNR in TSE images allowed better visualization of some PVSs as denoted by the arrows in the maximum (TSE) and minimum (MPRAGE) intensity projection images in Fig. 5.

Morphological features of PVS

The TSE images with TE = 319 ms were used for studying PVS morphological features as they had the highest rCNR. Figs. 6(A) and (B) show an example of a TSE image and the overlaid WM mask obtained from the MP2RAGE images, respectively. Most tubular structures can be extracted within the WM by applying the Frangi's vesselness filter as shown in Fig. 6(C). Some misclassified PVSs were removed by the

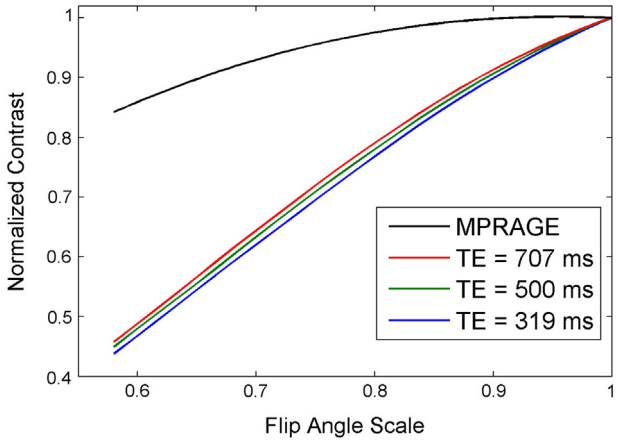

Fig. 3. The dependence of PVS–WM contrast on the flip angle scale in the simulation of B_1 inhomogeneity. The contrast is normalized by the value at the flip angle scale equal to 1.

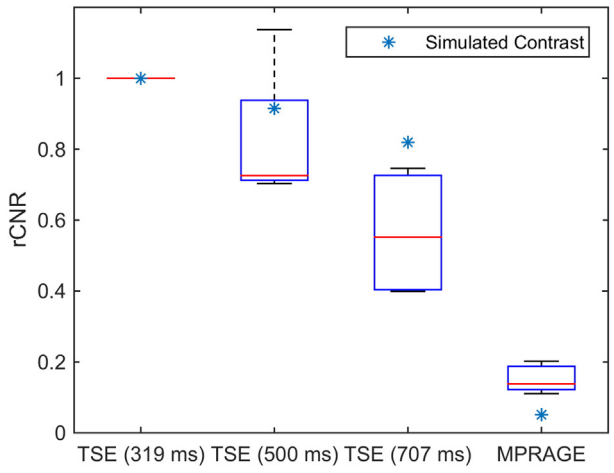

Fig. 4. Comparison of the experimental rCNR and simulated contrast between PVS and WM in the MPRAGE and TSE sequences. The results are normalized by the values for TSE with TE = 319 ms. The top, center, and bottom lines of boxes represent the upper quartile, median, and lower quartile values, respectively, and the upper and lower whiskers represent the maximum and minimum values, respectively.

length thresholding as denoted by the green arrows in Figs. 6(C) and (D). Finally, Fig. 6(E) shows the PVS mask after manual editing to correct for the misclassified voxels, including the true (white arrow) and false (yellow arrow) PVS voxels. A 3D rendering of the final segmented PVS along the inferior–superior axis is shown in Fig. 6(F).

A total of 208 ± 52, 287 ± 44, 21 ± 9, and 26 ± 8 (group mean ± group SD) PVSs were segmented in FL, POL, TL, and SN, respectively. The distributions of length, volume, and diameter for the PVS in the four regions are shown in Figs. 7(A)–(C). All these distributions are asymmetric around the peak and right-skewed. Figs. 7(E)–(G) are the boxplots showing the minimum, lower quartile, median, upper quartile, and the maximum values of the distributions. The length and volume distributions are almost identical in the three WM regions, although the distributions in TL have large errors due to the much smaller number of PVSs in TL. The PVSs in SN have overall smaller lengths and volumes than those in WM. Note that, due to the small field of view employed in the TSE scans, the image wrap-around from the top of head overlaps with 20 ±9% of the SN on the inferior side, thus making it impossible to delineate PVS in the affected regions. Therefore, the lengths and volumes of the subcortical PVS might be slightly underestimated. The diameter distributions of FL and POL PVSs are very similar, while those of TL and SN are slightly shifted to smaller and larger diameters, respectively. The mean diameters are 0.71 ± 0.03 mm, 0.72 ± 0.03 mm, 0.68 ± 0.06 mm, and 0.77 ± 0.04 mm in FL, POL, TL, and SN, respectively. F-test reveals significant difference ($p = 0.0065$) in the mean diameters among the four regions. Paired t-test also shows that the mean diameter in SN is significantly greater than the three WM regions ($p < 5.5 \times 10^{-3}$), while the mean diameters in the three WM regions are not significantly different ($p \geq 0.1$).

Fig. 7(D) shows the variation of mean PVS diameters along the PVS path. The diameter at normalized distance nearest to 0 is significantly larger than that nearest to 1 for POL (paired t-test, $p = 0.004$), while these two diameters were not statistically different for the other three regions ($p \geq 0.08$). The diameters significantly varied along the path in the three WM regions (F-test, $p \leq 0.03$), while the variation in SN is not statistically significant ($p = 0.26$). In WM, the PVS had the largest diameter around the center of the PVS.

Fig. 7(H) shows the volume fraction of PVS in the four regions. There was a significant difference in the volume fraction among the four regions (F-test, $p = 1.3 \times 10^{-6}$). Specifically, the POL had the highest volume fraction, while the TL had the least. Paired t-tests showed that all the volume fractions were significantly different between each other, except between FL and SN.

Discussion

In this paper, simulation and experimental evaluations of the CNR of T_1-weighted MPRAGE and T_2-weighted VFA-TSE sequences for visualization of PVS in the human brain were conducted at 7 T. Both simulation and experimental results show that TSE sequence provides a much higher CNR than MP-RAGE, which can be explained by two factors. First, the ratio of T_2 (=8.0) between PVS and WM is much greater than that of T_1 (=2.6), leading to a greater signal difference between the two tissues with a T_2-weighted sequence. Second, the MPRAGE sequence requires the use of a relatively small flip angle for the readout of magnetization during inversion recovery. For example, under the conditions used in our simulation, the maximum contrast is achieved with a flip angle of 8° (Fig. 2(C)), resulting in only 14% of the longitudinal magnetization being available for imaging. In contrast, the steady-state echo signal reaches 42.0%–54.4% of the fully relaxed magnetization for the TSE sequence, resulting in a higher signal.

It is well understood that the application of variable flip angles in TSE sequences will affect the spatial resolution of the images; the extent to which resolution is affected depends on the width of the point spread function (PSF) resulting from echo signal evolution. This potential effect on spatial resolution could be highly relevant for our study since a sufficiently high resolution is often needed to better discern normal PVS. To minimize the width of the PSF for PVSs and improve their visualization, the measured T_1 and T_2 of CSF were used for the calculation of variable flip angles, assuming similar T_1 and T_2 for CSF and PVS. On the other hand, the PSF for WM would be broadened due to our choices of T_1 and T_2 in the calculation. However, since the WM signal is much lower (<50%) compared to PVS, the image blurring effect on PVS due to WM contamination is expected to be small.

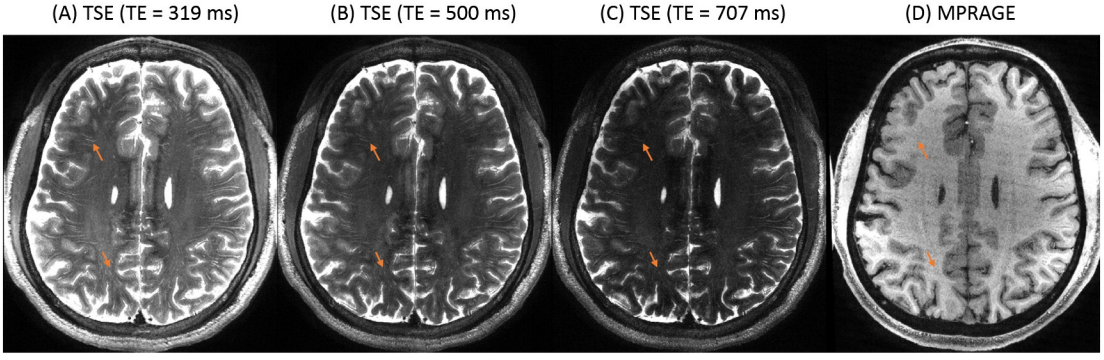

Fig. 5. Examples of (A–C) maximum intensity projection TSE and (D) minimum intensity projection MPRAGE images in the same subject that shows more visible PVS in the former and at shorter TE as denoted by the arrows. The echo times were 319 ms, 500 ms, and 700 ms in panels (A), (B), and (C), respectively. The projections were performed on 8 neighboring slices.

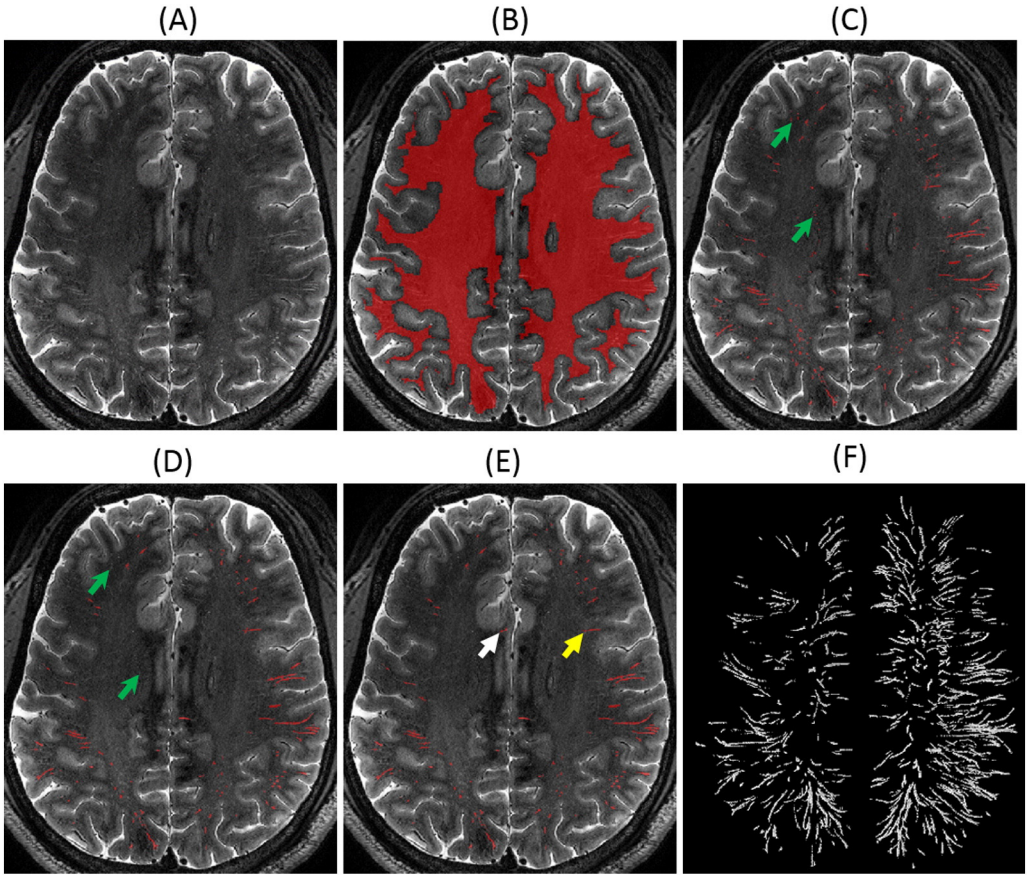

Fig. 6. Illustration of the PVS segmentation procedure. (A) A brain image slice with PVS. (B) Segmented WM (red). (C) Thin tubular structures obtained by Frangi's vesselness filter. (D) PVS mask after excluding clusters with the length less than 0.8 mm or greater than 30 mm. The green arrows indicate voxels that are removed by the length threshold. (E) PVS mask after manual editing. The white and yellow arrows indicate voxels that were manually added to and removed from the PVS mask, respectively. (F) A volume rendering of segmented PVS.

In our simulation, only the PVS–WM contrast was compared among different sequences, and the noise levels were assumed to be the same. Since ultra-high resolution images were acquired in our study, the image noise is most likely dominated by the thermal noise (Triantafyllou et al., 2005). The noise level can be different between MPRAGE and TSE images, due to differences in receiver bandwidth, matrix size, and partial Fourier factors (PFF). However, these factors are unlikely to account for the 10× differences in contrast between them. We also observed a TE dependence on PVS–WM CNR in the TSE images. For the TSE sequences with different TEs, the PFF were different and equaled

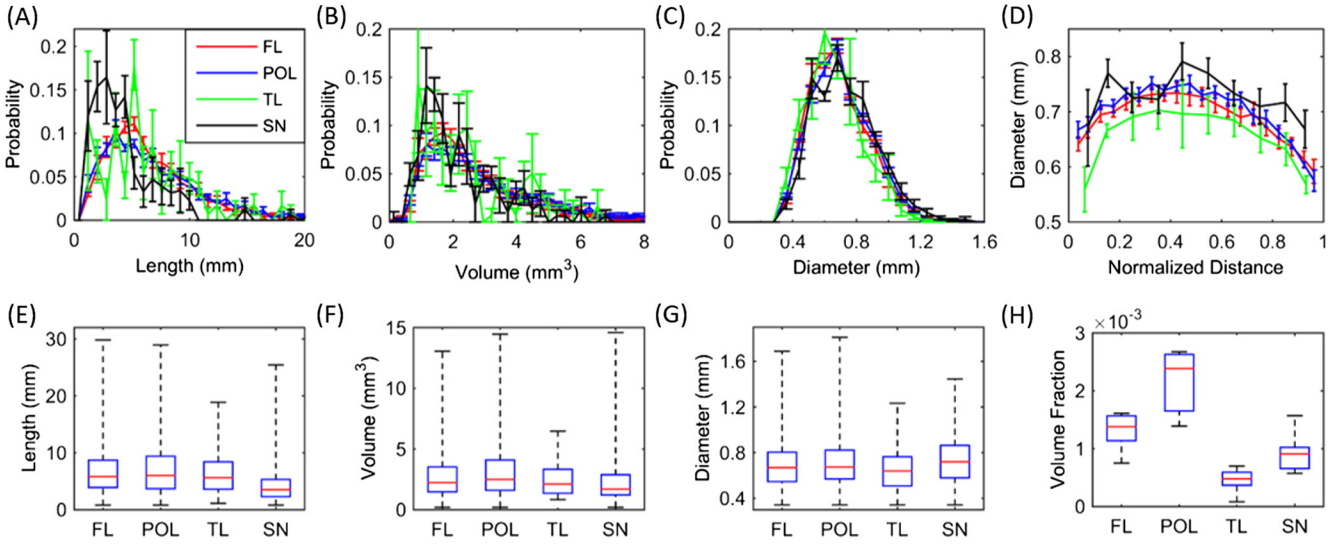

Fig. 7. Distributions of (A) length, (B) volume, and (C) diameter of PVS in the FL, POL, TL, and SN. (D) The variation of PVS diameters along the PVS paths in each of the four regions. The direction with increasing normalized distance corresponds to the direction of arterial blood flow inside PVS. In all graphs, the error bars denote the standard errors of the subject group mean. (E)–(G) Boxplots of the length, volume, and diameter distributions, respectively. (H) PVS volume fractions in the FL, POL, TL, and SN, respectively. The top, center, and bottom lines of each box represent the upper quartile, median, and lower quartile scores, respectively, while the upper and lower whiskers represent the maximum and minimum values, respectively.

to 74%, 88%, and 100% because a linear k-space sampling scheme was used. The effect of PFF on noise depends on the reconstruction algorithm and, in our case, the background noises between the three TE values were similar (in arbitrary units): 7.1 ± 0.3 (TE = 319 ms), 6.2 ± 0.5 (TE = 500 ms), and 7.3 ± 0.5 (TE = 707 ms). Therefore, the effect of PFF on noise can likely be ignored during TE optimization for CNR, which is further supported by the consistency between the simulation and experimental results in Fig. 4.

Due to B_1 inhomogeneity, our simulation showed a sequence-dependent reduction in CNR near the surface of the brain (Fig. 3). Thus, it is important to consider the potential effects of CNR reduction on our results, particularly the rCNR (Fig. 4) and morphological features (Fig. 7). First, there likely exist different degrees of CNR reduction in the three predefined WM regions, namely FL, POL, and TL regions, which can result in different sensitivities for PVS detection and contribute to the observed different PVS volume fractions (VF) in these three WM regions (Fig. 7H). Future studies with parallel transmitting coils providing a homogeneous B_1 field over the whole brain is necessary to further confirm the VF results (Katscher and Bornert, 2006). Second, the much less CNR reduction for the MPRAGE sequence at the same flip angle scale (Fig. 3) would increase the measured rCNR, which may explain the discrepancy between the theoretical and experimental rCNRs of MPRAGE in Fig. 4. However, the experimental rCNR results for the TSE sequences (Fig. 4) should not be affected since the CNR reduction has little dependence on TE.

On the other hand, the B_1 inhomogeneity is unlikely to affect the measured morphological distributions (Figs. 7(A)–(C)) and the observed diameter variations along the PVS paths (Fig. 7(D)). As most PVSs were less than 2 cm long, the CNR change over such a small distance is expected to be small. In fact, no noticeable systematic reduction in PVS–WM contrast near the brain surface was observed, as shown in Fig. 6(E). In addition, the length, volume, and diameter distributions of PVS are relatively homogeneous, despite potential differences in the degrees of B_1 reduction in the three predefined WM regions. Furthermore, although correction of image intensity variations due to B_1 inhomogeneity can improve tissue segmentations, such correction is unlikely to improve the PVS segmentation in the current study, since the vesselness is calculated based on local voxel intensities of a small neighborhood and is also independent of the overall absolute intensity in the neighborhood.

Our study revealed a non-monotonic variation of PVS diameters along their paths in WM, with the maximum diameter located near the middle of the PVS paths. This is surprising as the diameters of arterial vessels are expected to decrease when penetrating further into the brain parenchyma and the PVS and artery diameters are proportional to each other (Pesce and Carli, 1988). These results are also inconsistent with the findings reported in (Bouvy et al., 2014) where no caliber changes were observed in WM. Our result may be explained by the increased probability of tortuosity in the middle of the penetrating arterioles, which are accompanied by an associated increase in PVS diameter (Brown et al., 2002). The lack of caliber change in (Bouvy et al., 2014) might have resulted from insufficient spatial resolution, in which the voxel volume of the TSE sequence was 4.4 times larger than the current study. On the other hand, Bouvy et al. noticed focal dilations of PVS within 1 to 2 cm from the origin of lenticulostriate arteries in basal ganglia. While we also observed similar focal dilations for some PVS in SN (data not shown), the averaged results in Fig. 7(D) did not show significant variation along the paths, suggesting heterogeneous PVS diameter variation within the SN.

Consistent with (Bouvy et al., 2014), we did not observe any PVS in the cortex, either due to an insufficient CNR between cortex and PVS and/or insufficient spatial resolution. The reduced CNR can be caused by the B_1 inhomogeneity near the cortex as discussed above, while the insufficient spatial resolution can arise because PVS diameters close to the cortical surface is likely smaller than within the WM (Fig. 7(D)).

We used a simple geometric relation (Eq. (1)) for a cylinder to infer the diameters of PVS from their lengths and volumes. As the majority of PVSs have diameters that are less than twice the voxel size, some mismatch between the calculated and true PVS diameters is expected. In addition, some PVS segments with diameters much smaller than the voxel size cannot be detected. Therefore, the length and diameter distributions might be underestimated at values above and below their peak positions, respectively. Nevertheless, the distributions can still serve as a sensitive index for monitoring PVS morphological changes with age and in diseased populations, as long as the consistent imaging parameters and analysis methods are used across imaging sessions.

The large number of PVSs in the brain and their small diameters suggest that ultra-high resolution 3D imaging and semi-automatic segmentation approaches as developed in this study are necessary to characterize the morphological features of PVS. Our approach would allow accurate comparison of PVS morphology between subjects under different disease conditions or longitudinal studies of the enlargement of PVS with age or disease progression, which may provide new insights into the pathophysiological significance of PVS in neurovascular diseases.

Conclusions

In conclusion, the T_2-weighted VFA-TSE sequence had a much higher CNR for PVS visualization than the T_1-weighted MPRAGE sequence. The optimized T_2-weighted sequence with TE = 319 ms and 0.4 mm isotropic resolution enabled the visualization of a large number of PVSs in WM and SN in young healthy subjects. A semi-automatic method was developed to segment the PVS and reveal the detailed distributions of the length, volume, and diameter of PVS. Our approach enables accurate characterization of the morphological features of PVS, which may serve as a useful tool for understanding their pathophysiological significance in neurovascular diseases in which enlarged PVSs are observed.

References

Bender, B., Klose, U., 2010. The in vivo influence of white matter fiber orientation towards B(0) on T2* in the human brain. NMR Biomed. 23, 1071–1076.

Bilston, L.E., Fletcher, D.F., Brodbelt, A.R., Stoodley, M.A., 2003. Arterial pulsation-driven cerebrospinal fluid flow in the perivascular space: a computational model. Comput. Methods Biomech. Biomed. Engin. 6, 235–241.

Bouvy, W.H., Biessels, G.J., Kuijf, H.J., Kappelle, L.J., Luijten, P.R., Zwanenburg, J.J., 2014. Visualization of perivascular spaces and perforating arteries with 7 T magnetic resonance imaging. Investig. Radiol. 49, 307–313.

Brown, W.R., Moody, D.M., Challa, V.R., Thore, C.R., Anstrom, J.A., 2002. Venous collagenosis and arteriolar tortuosity in leukoaraiosis. J. Neurol. Sci. 203–204, 159–163.

Busse, R.F., Hariharan, H., Vu, A., Brittain, J.H., 2006. Fast spin echo sequences with very long echo trains: design of variable refocusing flip angle schedules and generation of clinical T_2 contrast. Magn. Reson. Med. 55, 1030–1037.

Conforti, R., Faella, P., Marrone, V., Iasiello, F., Di Maio, N., Rossi, C., Giganti, M., Santagata, M., 2013. Enlargement of Virchow–Robin spaces in cranial trauma: literature review. Recenti Prog. Med. 104, 318–321.

Conturo, T.E., Beth, A.H., Arenstorf, R.F., Price, R.R., 1987. Simplified mathematical description of longitudinal recovery in multiple-echo sequences. Magn. Reson. Med. 4, 282–288.

Cox, R.W., 1996. AFNI: software for analysis and visualization of functional magnetic resonance neuroimages. Comput. Biomed. Res. 29, 162–173.

Doubal, F.N., MacLullich, A.M., Ferguson, K.J., Dennis, M.S., Wardlaw, J.M., 2010. Enlarged perivascular spaces on MRI are a feature of cerebral small vessel disease. Stroke 41, 450–454.

Esiri, M.M., Gay, D., 1990. Immunological and neuropathological significance of the Virchow–Robin space. J. Neurol. Sci. 100, 3–8.

Frangi, A.F., Niessen, W.J., Vincken, K.L., Viergever, M.A., 1998. Multiscale vessel enhancement filtering. Medical Image Computing and Computer-Assisted Intervention—Miccai'98. 1496, pp. 130–137.

Hennig, J., 1988. Multiecho imaging sequences with low refocusing flip angles. J. Magn. Reson. 78, 397–407.

Iliff, J.J., Wang, M., Liao, Y., Plogg, B.A., Peng, W., Gundersen, G.A., Benveniste, H., Vates, G.E., Deane, R., Goldman, S.A., Nagelhus, E.A., Nedergaard, M., 2012. A paravascular pathway facilitates CSF flow through the brain parenchyma and the clearance of interstitial solutes, including amyloid beta. Sci. Transl. Med. 4, 147ra111.

Iliff, J.J., Wang, M., Zeppenfeld, D.M., Venkataraman, A., Plog, B.A., Liao, Y., Deane, R., Nedergaard, M., 2013. Cerebral arterial pulsation drives paravascular CSF-interstitial fluid exchange in the murine brain. J. Neurosci. 33, 18190–18199.

Inglese, M., Bomsztyk, E., Gonen, O., Mannon, L.J., Grossman, R.I., Rusinek, H., 2005. Dilated perivascular spaces: hallmarks of mild traumatic brain injury. AJNR Am. J. Neuroradiol. 26, 719–724.
Jenkinson, M., Bannister, P., Brady, M., Smith, S., 2002. Improved optimization for the robust and accurate linear registration and motion correction of brain images. Neuroimage 17, 825–841.
Katscher, U., Bornert, P., 2006. Parallel RF transmission in MRI. NMR Biomed. 19, 393–400.
Kress, B.T., Iliff, J.J., Xia, M., Wang, M., Wei, H.S., Zeppenfeld, D., Xie, L., Kang, H., Xu, Q., Liew, J.A., Plog, B.A., Ding, F., Deane, R., Nedergaard, M., 2014. Impairment of paravascular clearance pathways in the aging brain. Ann. Neurol. 76, 845–861.
Laule, C., Kozlowski, P., Leung, E., Li, D.K., Mackay, A.L., Moore, G.R., 2008. Myelin water imaging of multiple sclerosis at 7 T: correlations with histopathology. Neuroimage 40, 1575–1580.
Lee, J., van Gelderen, P., Kuo, L.W., Merkle, H., Silva, A.C., Duyn, J.H., 2011. T2*-based fiber orientation mapping. Neuroimage 57, 225–234.
Li, B.C., Li, Y., Xu, C., Wang, J., Chen, Z., Li, G., Zhang, J., Hu, S., Wang, L., Feng, H., 2014. Blast-induced traumatic brain injury of goats in confined space. Neurol. Res. 36, 974–982.
Longair, M.H., Baker, D.A., Armstrong, J.D., 2011. Simple neurite tracer: open source software for reconstruction, visualization and analysis of neuronal processes. Bioinformatics 27, 2453–2454.
Maclullich, A.M., Wardlaw, J.M., Ferguson, K.J., Starr, J.M., Seckl, J.R., Deary, I.J., 2004. Enlarged perivascular spaces are associated with cognitive function in healthy elderly men. J. Neurol. Neurosurg. Psychiatry 75, 1519–1523.
Marques, J.P., Kober, T., Krueger, G., van der Zwaag, W., Van de Moortele, P.F., Gruetter, R., 2010. MP2RAGE, a self bias-field corrected sequence for improved segmentation and T_1-mapping at high field. Neuroimage 49, 1271–1281.
Mugler III, J.P., Brookeman, J.R., 1990. Three-dimensional magnetization-prepared rapid gradient-echo imaging (3D MP RAGE). Magn. Reson. Med. 15, 152–157.
Pesce, C., Carli, F., 1988. Allometry of the perivascular spaces of the putamen in aging. Acta Neuropathol. 76, 292–294.
Potter, G.M., Doubal, F.N., Jackson, C.A., Chappell, F.M., Sudlow, C.L., Dennis, M.S., Wardlaw, J.M., 2013. Enlarged perivascular spaces and cerebral small vessel disease. Int. J. Stroke 10, 376–381.
Rangroo Thrane, V., Thrane, A.S., Plog, B.A., Thiyagarajan, M., Iliff, J.J., Deane, R., Nagelhus, E.A., Nedergaard, M., 2013. Paravascular microcirculation facilitates rapid lipid transport and astrocyte signaling in the brain. Sci. Rep. 3, 2582.
Rouhl, R.P., Damoiseaux, J.G., Lodder, J., Theunissen, R.O., Knottnerus, I.L., Staals, J., Henskens, L.H., Kroon, A.A., de Leeuw, P.W., Tervaert, J.W., van Oostenbrugge, R.J., 2012. Vascular inflammation in cerebral small vessel disease. Neurobiol. Aging 33, 1800–1806.
Sled, J.G., Zijdenbos, A.P., Evans, A.C., 1998. A nonparametric method for automatic correction of intensity nonuniformity in MRI data. IEEE Trans. Med. Imaging 17, 87–97.
Smith, S.M., 2002. Fast robust automated brain extraction. Hum. Brain Mapp. 17, 143–155.
Triantafyllou, C., Hoge, R.D., Krueger, G., Wiggins, C.J., Potthast, A., Wiggins, G.C., Wald, L.L., 2005. Comparison of physiological noise at 1.5 T, 3 T and 7 T and optimization of fMRI acquisition parameters. Neuroimage 26, 243–250.
Vaughan, J.T., Garwood, M., Collins, C.M., Liu, W., DelaBarre, L., Adriany, G., Andersen, P., Merkle, H., Goebel, R., Smith, M.B., Ugurbil, K., 2001. 7 T vs. 4 T: RF power, homogeneity, and signal-to-noise comparison in head images. Magn. Reson. Med. 46, 24–30.
Wardlaw, J.M., 2010. Blood–brain barrier and cerebral small vessel disease. J. Neurol. Sci. 299, 66–71.
Whittall, K.P., MacKay, A.L., Graeb, D.A., Nugent, R.A., Li, D.K., Paty, D.W., 1997. In vivo measurement of T_2 distributions and water contents in normal human brain. Magn. Reson. Med. 37, 34–43.
Wuerfel, J., Haertle, M., Waiczies, H., Tysiak, E., Bechmann, I., Wernecke, K.D., Zipp, F., Paul, F., 2008. Perivascular spaces—MRI marker of inflammatory activity in the brain? Brain 131, 2332–2340.
Yang, L., Kress, B.T., Weber, H.J., Thiyagarajan, M., Wang, B., Deane, R., Benveniste, H., Iliff, J.J., Nedergaard, M., 2013. Evaluating glymphatic pathway function utilizing clinically relevant intrathecal infusion of CSF tracer. J. Transl. Med. 11, 107.
Yushkevich, P.A., Piven, J., Hazlett, H.C., Smith, R.G., Ho, S., Gee, J.C., Gerig, G., 2006. User-guided 3D active contour segmentation of anatomical structures: significantly improved efficiency and reliability. Neuroimage 31, 1116–1128.
Zhang, Y., Brady, M., Smith, S., 2001. Segmentation of brain MR images through a hidden Markov random field model and the expectation–maximization algorithm. IEEE Trans. Med. Imaging 20, 45–57.
Zhu, Y.C., Dufouil, C., Mazoyer, B., Soumare, A., Ricolfi, F., Tzourio, C., Chabriat, H., 2011. Frequency and location of dilated Virchow–Robin spaces in elderly people: a population-based 3D MR imaging study. AJNR Am. J. Neuroradiol. 32, 709–713.